Bayesian framework for inversion of second-order stress glut moments: application to the 2020 M_w7.7 Caribbean Earthquake

James Atterholt[1] and Zachary E. Ross[1]

[1]Seismological Laboratory, California Institute of Technology, Pasadena, California, USA 91125

Key Points:

- We develop a Bayesian inverse scheme to solve for stress glut second moments of earthquakes using teleseismic data.
- We sample the positive-definite constrained posterior distribution using Hamiltonian Monte Carlo sampling and automatic differentiation.
- Using the 2020 M_w7.7 Caribbean Earthquake as an example, we demonstrate the efficacy and utility of this inverse framework.

Corresponding author: James Atterholt, atterholt@caltech.edu

Abstract

We present a fully Bayesian inverse scheme to determine second moments of the stress glut using teleseismic earthquake seismograms. The second moments form a low-dimensional, physically-motivated representation of the rupture process that captures its spatial extent, source duration, and directivity effects. We determine an ensemble of second moment solutions by employing Hamiltonian Monte Carlo and automatic differentiation to efficiently approximate the posterior. Our method explicitly constrains the parameter space to be symmetric positive definite, ensuring the derived source properties have physically meaningful values. The framework accounts for the autocorrelation structure of the errors and incorporates hyperpriors on the uncertainty. We validate the methodology using a synthetic test and subsequently apply it to the 2020 M_w7.7 Caribbean earthquake. The second moments determined for this event indicate the rupture was nearly unilateral and relatively compact along-strike. The solutions from this inverse framework can resolve ambiguities between slip distributions with minimal a priori assumptions on the rupture process.

Plain Language Summary

Earthquake science is presented with the challenging problem of determining properties of earthquake sources that occur deep within the Earth using observations made at the surface of the Earth. Typically, the process for determining these important quantities involves finding solutions to complicated optimization problems that, given the necessarily poor data coverage, are poorly constrained. With this challenge in mind, we present a framework to solve for some fundamental properties of earthquake sources like spatial extent, rupture propagation direction, and duration. This approach requires few assumptions about the geometry of the fault that ruptured and the dynamics of the rupture process, in contrast to more traditional methods. This procedure also provides a probabilistic description of these earthquake source properties, which is essential, because the uncertainty inherent to this problem dictates that we cannot confidently choose any one particular solution. We demonstrate this method's utility by applying it to the 2020 Magnitude 7.7 Caribbean Earthquake. Through this application, we show that this framework can both determine properties of earthquake sources that have historically been difficult to constrain and successfully resolve ambiguities between solutions of more traditional techniques.

Introduction

Earthquakes are complicated physical processes that dynamically vary in space and time. Better understanding the factors that control earthquake behavior consequently requires constraining the finite source properties of earthquakes. In pursuit of this understanding, high dimensional estimates of finite source properties are routinely computed for significant earthquakes (e.g. Wald & Heaton, 1992; Ammon, 2005; M. Moreno et al., 2010; Ide et al., 2011; Ross et al., 2019). These estimates usually involve the inversion for slip on a predefined fault plane using some combination of seismic, geodetic, and tsunami data with kinematic constraints placed on the rupture propagation (Hartzell & Heaton, 1983; Du et al., 1992; Saito et al., 2011). These solutions, termed fault slip distributions, are valuable in that they provide a detailed image of time-dependent slip behavior. But, the necessary user-defined parameterization, general lack of sensitivity to rupture velocity, and necessary regularization makes these estimates of finite source properties strongly nonunique (e.g. Lay, 2018). This nonuniqueness presents challenges to objectively comparing finite source properties between events, and thus limits our ability to discern patterns in earthquake behavior that could inform a deeper understanding of earthquake phenomenology.

The limitations of routinely computed estimates of finite source properties motivates the development of alternative estimates that overcome these limitations. One potential alternative is the second moment formulation (G. Backus & Mulcahy, 1976a, 1976b), in which higher-order mathematical moments of the stress glut, a source representational quantity, are used to describe basic properties of the rupture process in space and time. Higher-order stress glut moments have been successfully computed in the past (Bukchin, 1995; McGuire et al., 2000, 2001, 2002; McGuire, 2004; Chen, 2005; Meng et al., 2020), but this methodology has received little attention compared to slip inversions. The second-moment formulation yields low-dimensional, physically-motivated estimates of the spatial extent, directivity, and duration of earthquake ruptures. It requires no prior knowledge of the rupture velocity, and makes only mild assumptions about the source geometry. Being free of gridding and associated discretization issues that complicate slip inversions, the second moment formulation can more objectively facilitate comparisons between events, helping to find common patterns. Illuminating these patterns may help address outstanding questions in earthquake science relating to how fault zones may facilitate or impede earthquake ruptures.

Our contributions in this paper are as follows. We develop a Bayesian inverse scheme for second moments using teleseismic data. We employ Hamiltonian Monte Carlo sampling and automatic differentiation to efficiently sample from the posterior distribution. In doing so, we apply a set of transformations that ensure positive definiteness of the second moments. We demonstrate the efficacy of our methodology by applying the inversion scheme to the 2020 M_w7.7 Caribbean Earthquake. We show that our methodology is useful for both inferring source parameters that are poorly constrained by other source estimation procedures and resolving ambiguities between finite slip distributions.

Case study: the 2020 M_w7.7 Caribbean earthquake

Event background and tectonic summary

On January 28, 2020, a large earthquake occurred in the Caribbean Sea near the Cayman Islands. The global Centroid Moment Tensor (gCMT) (Dziewonski et al., 1981; Ekström et al., 2012) solution of this earthquake suggests that the event was a largely double-couple, nearly vertically dipping, strike-slip earthquake with a moment magnitude of M_w7.7 (GCMT, 2020). The geographic setting of this event is shown in Figure 1. This event took place near the northern margin of the Gonâve Microplate, an elongated plate that characterizes a portion of the boundary between the North American and Caribbean plates. The dominant local structural feature in this region is the Mid-Cayman Rise, which produces seafloor spreading that is partially accommodated by the transform faults that bound the Gonâve Microplate (Mann et al., 1995; DeMets & Wiggins-Grandison, 2007). The centroid location and focal mechanism of the Caribbean Earthquake suggest that this event likely ruptured the Oriente Fault, a left-lateral transform fault that constitutes the boundary between the North American Plate and the Gonâve Microplate. Though the spreading rate of the Mid-Cayman Rise is slow (DeMets & Wiggins-Grandison, 2007), the segments of the Oriente Fault neighboring the Caribbean Earthquake have produced numerous M6+ earthquakes in recent history (Van Dusen & Doser, 2000; B. Moreno et al., 2002).

Despite its large magnitude, there are few finite rupture solutions for the Caribbean Earthquake to date (USGS, 2020; Tadapansawut et al., 2021). Though these solutions agree that the Caribbean earthquake likely ruptured unilaterally to the SW along the Oriente Fault, there is no consensus on some fundamental source parameters, such as the rupture's lateral extent. In particular, the USGS solution for this event suggests that most of the slip was confined within an 80 km length along the fault, while the Tadapansawut et al. solution suggests a much larger slip region that extends well over 300 km. Thus, in addition to producing statistically robust estimates of rupture characteristics, this second moment formulation may prove useful in resolving first-order differences between slip distributions.

Data

In this study we use vertical component seismic data from 52 Global Seismographic Network (GSN) stations (Figure 1). We selected these stations by evaluating how well the waveforms were approximated by point source synthetics computed using the gCMT solution. The seismograms used in the inversion are 700 second windows about the surface wave packet that we manually selected from 7200 second windows that start at the gCMT centroid time for the Caribbean Earthquake. We down-sample the waveform data to 0.1 Hz sampling rate to somewhat reduce the correlation between samples, while keeping computational demands minimal. As part of the construction of the forward propagation matrix, we computed the Green's tensor using the gCMT moment tensor and centroid location, which we perturbed to compute the requisite spatial derivatives numerically.

Methodology

Stress Glut Moments

Because an earthquake is constituted by a localized zone of inelastic deformation, we can represent the source region as a localized departure from elasticity. These departures can be quantified using the so-called stress glut, $\mathbf{\Gamma}$, the tensor field computed by applying an idealized Hooke's law to the inelastic component of strain in a system (G. Backus & Mulcahy, 1976a, 1976b). The stress glut is nonzero only within the source region. The stress glut is a complete representation of a seismic source in space and time that can be used to reproduce displacements everywhere on Earth for an arbitrary source (Dahlen & Tromp, 1998). Given the typically sparse distribution of seismic observations, solving for the full stress glut is an ill-posed problem. We can simplify the stress glut by assuming the source geometry is constant in space and time:

$$\mathbf{\Gamma}_{ij}(\xi,\tau) = \hat{\mathbf{M}}_{ij} f(\xi,\tau) \tag{1}$$

Where is $\hat{\mathbf{M}}$ is the normalized mean seismic moment tensor and f is the scalar function. This approximation reduces the solution from a tensor field to a scalar field and is most valid for seismic sources with stable source mechanisms.

We can further reduce the dimensionality of the stress glut by first recognizing that any scalar function in a bounded interval may be uniquely determined by its collection of polynomial moments. Because f captures a static displacement, f is nonzero for infinite time and thus occupies an unbounded interval, but $\dot{f}$ vanishes to zero at the cessation of rupture and is thus captured within a bounded interval. Hence, considering that the stress glut prescribes displacements due to an arbitrary seismic source, we can represent seismic displacements as the superposition of the spatio-temporal moments of the rate function $\dot{f}$. At low frequencies, we can truncate this infinite series such that we only include terms with moments of order $m+n \leq 2$. We can then explicitly define the measured displacements for a station i at low frequencies as:

$$\begin{aligned} u_i(\mathbf{r},t) \quad = \quad & \dot{f}^{(0,0)}(\xi_c,\tau_c)\mathbf{M}_{jl}\frac{d}{d\xi_l}\int_{-\infty}^{+\infty}\mathbf{G}_{ij}(\xi_c,\tau_c,\mathbf{r},t)dt \\ & -\dot{f}_m^{(1,1)}(\xi_c,\tau_c)\mathbf{M}_{jl}\frac{d}{d\xi_m}\frac{d}{d\xi_l}\mathbf{G}_{ij}(\xi_c,\tau_c,\mathbf{r},t) \\ & +\frac{1}{2}\dot{f}_{mn}^{(2,0)}(\xi_c,\tau_c)\mathbf{M}_{jl}\frac{d}{d\xi_m}\frac{d}{d\xi_n}\frac{d}{d\xi_l}\int_{-\infty}^{+\infty}\mathbf{G}_{ij}(\xi_c,\tau_c,\mathbf{r},t)dt \\ & +\frac{1}{2}\dot{f}^{(0,2)}(\xi_c,\tau_c)\mathbf{M}_{jl}\frac{d}{d\xi_l}\frac{d}{dt}\mathbf{G}_{ij}(\xi_c,\tau_c,\mathbf{r},t) \end{aligned} \tag{2}$$

Where $\mathbf{G}$ is a Green's tensor prescribing the path effects from a source with the centroid location ξ_c and centroid time τ_c to an arbitrary station with the location $\mathbf{r}$ at time t, and $\dot{f}^{(m,n)}(\xi_\mathbf{c},\tau_c)$ is the moment of the scalar rate function $\dot{f}(\xi,\tau)$ of spatial order m and temporal order n taken about the source centroid in space and time (Bukchin, 1995).

Several of the moments are of routine use in seismology, while the rest are worked with sparingly. The moment of order $m+n=0$ is the scalar moment of the source. The moments of order $m+n=1$ correspond to the spatial ($m=1$) and temporal ($n=1$) centroids of the source. Perhaps unfamiliar are the moments of order $m+n=2$; these moments describe low-dimensional finite properties of earthquake sources. In particular, $\dot{f}^{(2,0)}(\xi_\mathbf{c},\tau_c)$ is the spatial covariance of the stress glut, $\dot{f}^{(1,1)}(\xi_\mathbf{c},\tau_c)$ is the spatio-temporal covariance of the stress glut, and $\dot{f}^{(0,2)}(\xi_\mathbf{c},\tau_c)$ is the temporal variance of the stress glut. These so-called second moments yield low-dimensional, physically-motivated approximations of the source volume, source directivity, and source duration respectively (G. E. Backus, 1977).

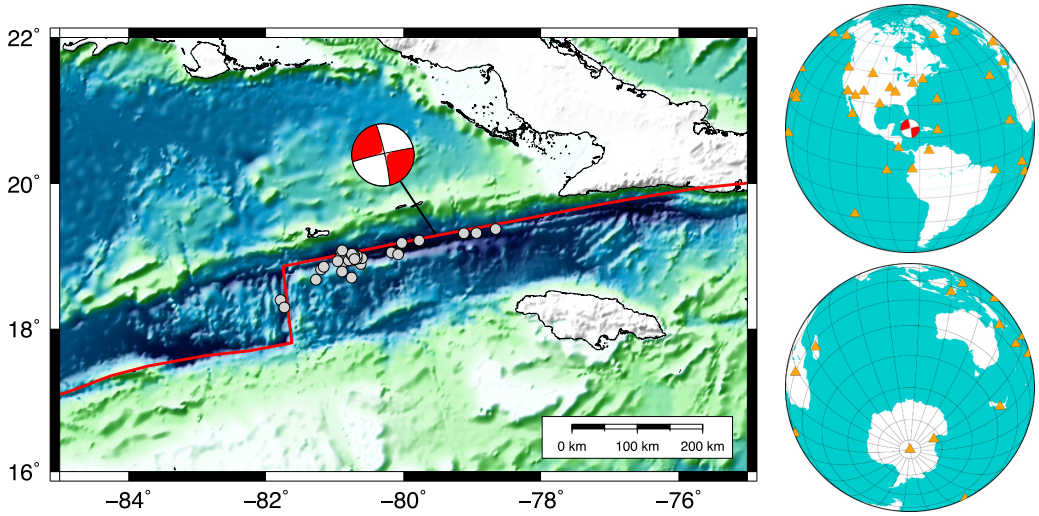

Figure 1. Left: Geographic setting of the 2020 Caribbean earthquake. Focal mechanism is the gCMT solution for the 2020 Caribbean earthquake. Gray dots indicate the locations of USGS cataloged aftershocks for the event. Red line indicates the boundary between the North American and Caribbean plates (Bird, 2003). Map coloring is reflective of seafloor depth. Right: Global distribution of stations from which waveforms were used in this study.

Waveform preprocessing

To compute the Green's tensor, we use the Preliminary Reference Earth Model (PREM) (Dziewonski & Anderson, 1981) and the normal mode summation package Mineos (Masters et al., 2011). To improve stability when approximating integrals and derivatives, we compute this Green's tensor at a high sampling rate (20 Hz). We take the necessary temporal and spatial derivatives and integrals of this Green's tensor numerically using a centered finite difference approximation. For the spatial derivatives, the finite difference offsets from the spatial centroid are 250 m. The construction of the forward propagation matrix described in this study require both the gCMT moment tensor and the Green's tensor derivatives and integrals.

We bandpass the observed waveforms and green tensor between 100 and 200 seconds and perform a visual quality control by comparing the displacements of the synthetic point source representation of our source with the observed waveforms. Because the contribution of moments of order $m + n \geq 2$ should be small, the synthetic waveforms produced using a point source approximation should be similar to the observed waveforms. We thus remove stations that did not show a good match between the synthetic point source displacements and the observed waveforms. We then align the Green's tensor and observed displacements of the remaining stations via cross correlation, and we manually pick the arrivals of and determine the window lengths for the surface wave packets at each station. These windows constitute the time-segments of the Green's tensor and observed waveforms included in the forward propagation matrix and data vector used in this study respectively.

The Inverse Problem

Though equation 2 appears unruly, many of the terms that constitute it are easily accessible. For a given source, we can observe $u_i(\mathbf{r}, t)$ using seismic instrumentation; we can solve for $\mathbf{G}$, $\mathbf{M}$, and $(\xi_{\mathbf{c}}, \tau_c)$ using routine techniques; and we can compute the necessary derivatives and integrals using numerical methods. Thus, in equation 2, only the moments

of the scalar function $\dot{f}$ are unknown. We can then pose equation 2 as a linear inverse problem:

$$\mathbf{d} = \mathbf{F}\mathbf{p} \tag{3}$$

where $\mathbf{d}$ is a vector of measured displacements, $\mathbf{F}$ is a forward propagation matrix of spatial and temporal integrals and derivatives of $\mathbf{G}$, the columns of which are weighted by the components of $\mathbf{M}$, and $\mathbf{p}$ is a vector of parameters which constitute the lower-order moments of the stress glut.

Numerous Bayesian methods for source parameter inversion have been proposed for problems such as focal mechanism estimation (Wéber, 2006; Walsh et al., 2009; Lee et al., 2011; Duputel et al., 2014) and slip distribution estimation (Monelli et al., 2009; Minson et al., 2013). Bayesian approaches for source estimation are growing in popularity because the probabilistic nature of these inversions is such that they do not require the user to choose a single solution for problems that, due to uncertainty, have many potential solutions. Instead, Bayesian approaches provide ensembles of solutions that are informed by prior distributions determined by physical constraints or ground truth. The Bayesian formulation described here allows for the computation of an ensemble of solutions for second moments that represent distributions of potential low-dimensional finite source properties for an earthquake source.

The posterior distribution for this problem can be written as follows (e.g. Tarantola, 2005),

$$p(\mathbf{p}, \sigma|\mathbf{d}) \propto p(\mathbf{d}|\sigma, \mathbf{p})\; p(\sigma)\; p(\mathbf{p}), \tag{4}$$

where σ is a hyperparameter. For the likelihood term, $p(\mathbf{d}|\sigma, \mathbf{p})$, we use a multivariate normal distribution,

$$p(\mathbf{d}|\sigma, \mathbf{p}) \propto \frac{1}{\sqrt{|\Sigma|}} \exp(-\frac{1}{2}(\mathbf{d} - \mathbf{F}\mathbf{p})^T\, \mathbf{\Sigma}^{-1}\, (\mathbf{d} - \mathbf{F}\mathbf{p})) \tag{5}$$

Since the observations are time-series data, errors in the forward model will result in temporal autocorrelation. We can account for this correlation structure through the data covariance matrix, $\mathbf{\Sigma}$, as outlined in (Duputel et al., 2014). If both points d_i and d_j are recorded by the same station:

$$\mathbf{\Sigma}_{ij} = \sigma \cdot \exp(-|i - j|\delta t/\Delta t) \tag{6}$$

Where δt is the sampling rate, and Δt is the shortest period information included in the time-series. This correlation structure accounts for temporal correlation in the errors, but not any spatial correlation. In this paper we assume that the observations are spatially distributed sparsely enough that spatially-correlated errors are negligible.

We use uninformed priors in this case study. But, this framework is flexible such that informed priors can easily be incorporated (Gelman et al., 2010). That is, with the physical interpretation of the second moment properties that we will describe shortly, priors on the spatial extent, directivity, and duration may be imposed given observational ground truth. For example, if the true nodal plane of an earthquake is known, Gaussian priors may be placed on the spatial second moment parameters to restrict the principal eigenvector of the spatial covariance matrix to abut the true nodal plane.

The total number of parameters in this inverse problem is 11, and we approximate $p(\mathbf{p}, \sigma|\mathbf{d})$ using Markov Chain Monte Carlo (MCMC) sampling to obtain an ensemble of solutions. We do not solve for the zeroth or first order moments, and instead use the gCMT solution as our moment tensor and centroid location. Because the parameter space is quite large, we sample the posterior distribution using Hamiltonian Monte Carlo (HMC) sampling (Neal, 2010), which is an instance of the Metropolis-Hastings algorithm that can efficiently sample large parameter spaces using principles from Hamiltonian dynamics. This

is accomplished in part by incorporating gradient information into the sampling process; however, it requires a means to also compute gradients efficiently. Here, we accomplish this through the use of reverse-mode automatic differentiation (Innes, 2019).

For each chain in this inversion, we draw 5000 samples from the posterior distributions after drawing 5000 burn-in samples. In this inversion, the momentum distribution has a diagonal mass matrix and the samples are updated using an ordinary leapfrog integrator (Neal, 2010). The only hyperparameter in this inversion is σ, which we use to construct the covariance matrix according to equation 6. To evaluate convergence, we run at least 3 chains of the inversion and compute the Gelman-Rubin diagnostic using the computed set of chains (Gelman & Rubin, 1992). That is, we compare the variability within chains to the variability between chains to determine if the chains all converge to the same target distributions.

Additionally, because the second moments of the stress glut are covariances, only a subset of the parameter space produces valid solutions. Specifically, the second moments are symmetric positive definite,

$$\mathbf{X} = \begin{bmatrix} \dot{f}^{(2,0)}(\xi_{\mathbf{c}}, \tau_c) & \dot{f}^{(1,1)}(\xi_{\mathbf{c}}, \tau_c) \\ \dot{f}^{(1,1)}(\xi_{\mathbf{c}}, \tau_c)^T & \dot{f}^{(0,2)}(\xi_{\mathbf{c}}, \tau_c) \end{bmatrix} \succeq 0. \tag{7}$$

Physically, this is equivalent to saying that the spatial extent and duration of the source are both non-negative. Typically, when performing a constrained Bayesian inversion, the easiest course of action is to sample under an unconstrained parameter space and subsequently transform those parameters into the necessarily constrained parameter space (Gelman et al., 2010). To this end, we note that, by the Cholesky Factorization Theorem, every symmetric positive-definite matrix can be decomposed into the product of some lower triangular matrix with a positive diagonal and the transpose of that same lower triangular matrix. This means that given $\mathbf{X}$, there exists a lower triangular matrix $\mathbf{L}$ with positive diagonal components such that:

$$\mathbf{X} = \mathbf{L}\mathbf{L}^T \tag{8}$$

Thus, we can sample freely from the unconstrained off-diagonal components of $\mathbf{L}$ and from the natural logarithm of the diagonal components of $\mathbf{L}$. Then, to evaluate our sample against our data, we can simply build $\mathbf{L}$ using our sample components and then construct $\mathbf{X}$ using equation 5. From $\mathbf{X}$ we can extract a valid $\mathbf{p}$ with which we evaluate the likelihood of our sample. A keen observer may notice that while $\mathbf{X}$ need only be symmetric positive semi-definite, the Cholesky factorization forces $\mathbf{X}$ to be positive definite. In practice, this distinction is inconsequential, as a positive semi-definite $\mathbf{X}$ suggests that at least one dimension of the source is identically zero, which will never be true in reality.

Results

Before showing the application of this methodology to real data, we will show a test of the outlined inversion procedure using a synthetic source. We can also use this test to determine the resolvability of the parameters of the Caribbean earthquake. To these ends, we prescribe a 60x20 km rectangular fault with a strike and dip corresponding to the nodal plane of the gCMT solution that is aligned with the Oriente Fault. We then define a grid of point sources, each with the gCMT source mechanism and equal fraction of the gCMT moment, along this prescribed fault such that the spatial release of moment can be approximated as uniform distributions of moment release along the strike and dip of the fault. We delay the activation of these point sources according to a prescribed rupture velocity of 1.2 km/s along strike, resulting in an event duration of 50 s, such that the moment release with time can also be approximated as a uniform distribution. Using the fact that the width of a uniform distribution is equal to $2\sqrt{3}\sigma$, where σ is the standard deviation of the Gaussian approximation of that uniform distribution, we can determine the true second moment solution for this synthetic source. In the interest of evaluating the resolvability of parameters for the Caribbean earthquake, we invert for these second moments using the same distribution of stations and the same windowing procedure that we use for the real event. For this test, we also use the mean σ from the inversion of real data so we could assess how visible known features are in the presence of realistic error. The joint probability distributions for each pair of inverted parameters are shown in Figure 7. These plots show that most of the parameters are either uncorrelated or weakly correlated with each other, with the exception of some of the spatio-temporal terms with their spatial counterparts and some closely related spatial terms.

We can further test the fidelity of our inversion results by computing synthetic waveforms using equation 2 and evaluating the fit to the observed waveforms generated for this synthetic example. The waveforms for an ensemble of second moment solutions from a single chain for the synthetic test are shown for a subset of stations with a large diversity of azimuths and distances in Figure 3. The waveform fits match the synthetic observations very well, particularly when the full ensemble of solutions is considered.

In order to represent the second moment solutions for the synthetic test in a more physically interpretable way, we convert the second moments into measures of volume, directivity, and duration. To estimate the volume of moment release from this source, we define an ellipsoid using the eigenvalues and eigenvectors of the spatial second moment of the event, $\dot{f}^{(2,0)}(\xi_{\mathbf{c}}, \tau_c)$. Assuming the spatial moment distribution follows a 3-dimensional Gaussian function, this ellipsoid represents the volume encompassing 95% of the moment released during the earthquake. The projections of the ellipsoids for the ensemble of solutions from a single chain from the synthetic test are shown in Figure 4. We can also infer the instantaneous velocity of the moment centroid, an estimate of directivity, by dividing the spatiotemporal second moment of the source, $\dot{f}^{(1,1)}(\xi_{\mathbf{c}}, \tau_c)$, by the temporal second moment of the source, $\dot{f}^{(0,2)}(\xi_{\mathbf{c}}, \tau_c)$. The map-view projections and Z-components of these velocity vectors for the synthetic test are given in Figure 4. Finally, we can estimate the source duration if we assume the moment rate function of the earthquake is a Gaussian distribution about the temporal centroid. Then, the second temporal moment of the source, $\dot{f}^{(0,2)}(\xi_{\mathbf{c}}, \tau_c)$, defines the variance of that moment-rate function. These Gaussian approximations to the moment-rate function for the synthetic test are plotted in Figure 4. Figure 4 also allows us to evaluate how well the ensemble of solutions captures the true solution for this test. Indeed, the true along-strike length, vertical extent, directivity, and duration all fall within the ensemble of solutions which suggests these are well constrained features in this inversion.

Now, we invert for the second moments of the 2020 Caribbean event using the real data. The distributions of the 10 independent parameters of the second moments for a single chain of the inversion using the real data are shown in Figure 5. We run the inversion for a set of chains, shown in Figure S1, and compute the Gelman-Rubin diagnostic (Gelman & Rubin,

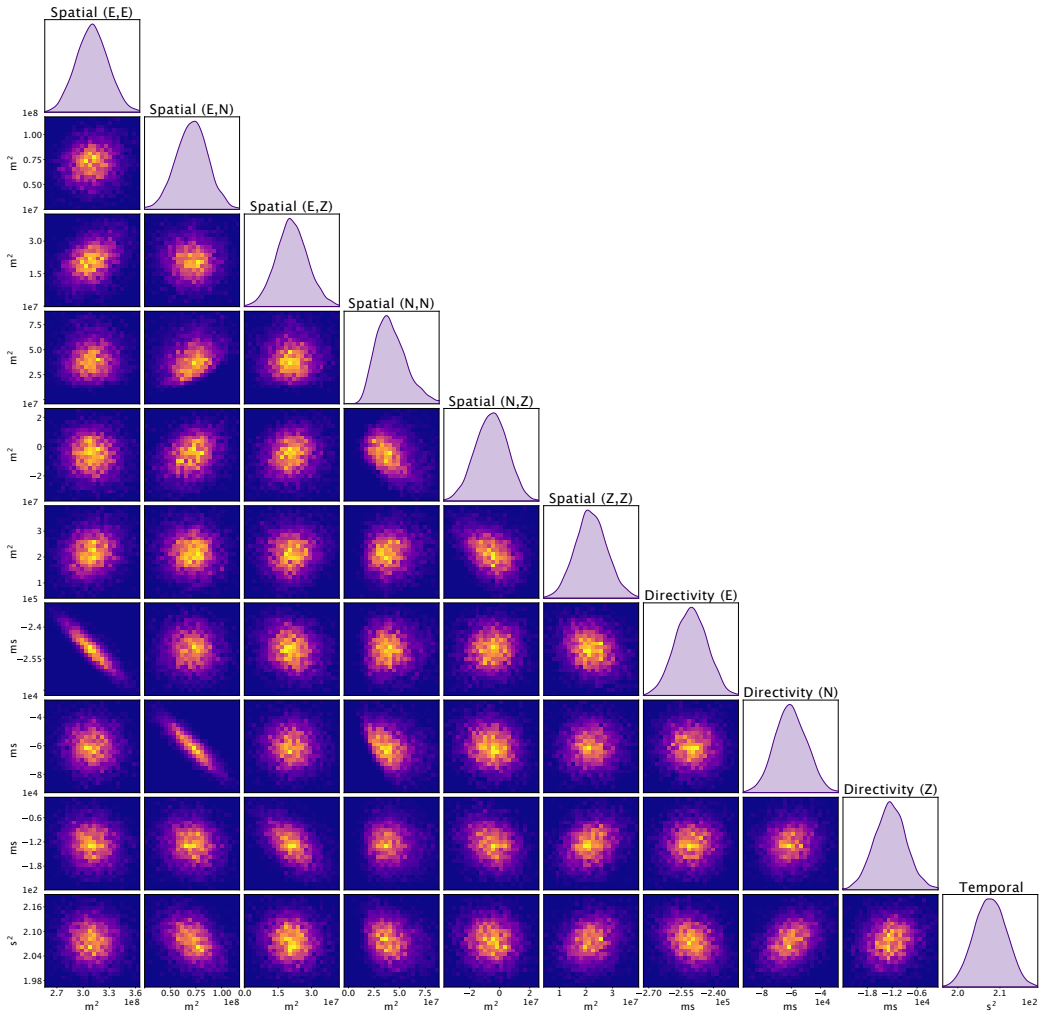

Figure 2. Marginal and joint probability density plots for the 10 independent parameters inverted for the synthetic test in this study. Off-diagonal plots are 2-dimensional histogram plots representing the joint probability distribution for each pair of independent parameters. On-diagonal plots are kernel density estimate plots for the marginal distributions of the adjacent joint probability distributions.

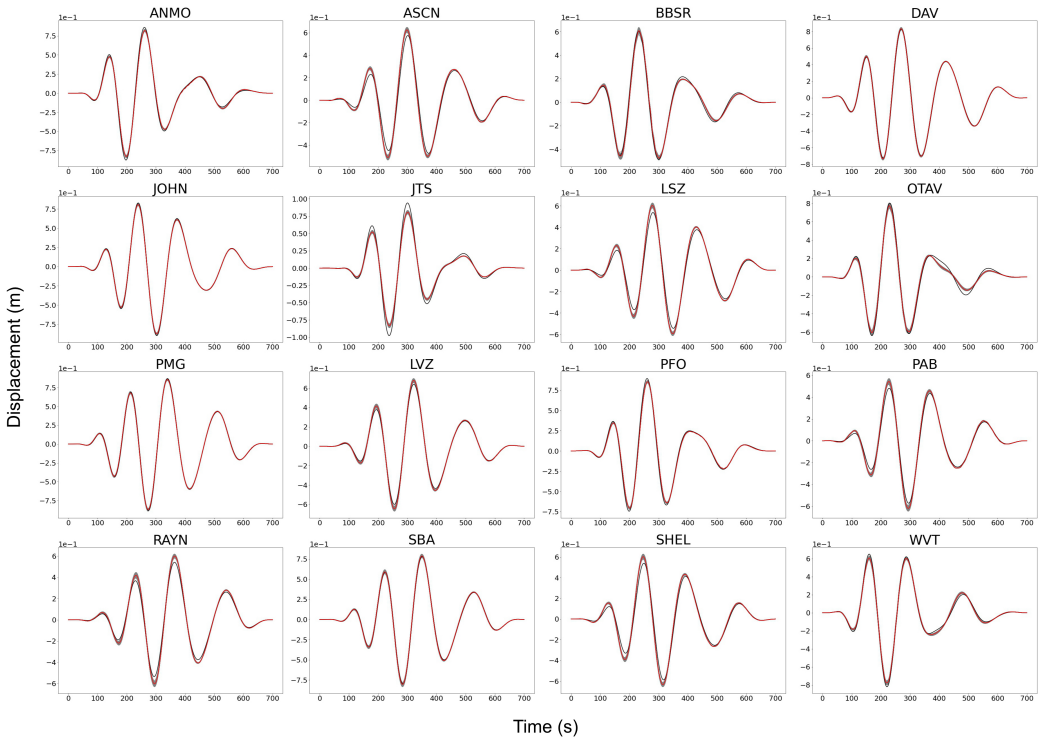

Figure 3. Waveform fits for a subset of the windowed waveforms for the synthetic test conducted in this study. Waveforms are labeled according to the GSN station at which they were generated. Black waveforms are synthetic observations. Gray waveforms are generated using a single solution from the ensemble of solutions from our inversion. Waveforms from each solution in the ensemble are plotted. Red waveforms are generated using the mean solution of the ensemble of solutions from our inversion.

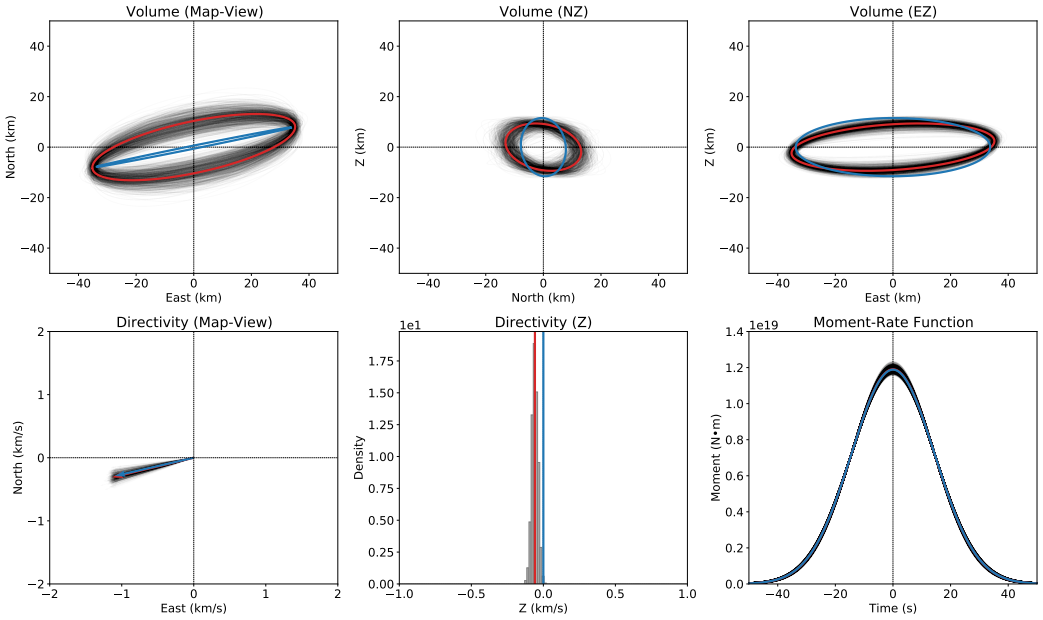

Figure 4. Physically motivated representation of the ensemble of second moment solutions for the synthetic test. Top row: Projections of the spatial ellipsoid generated using the eigenvalues and eigenvectors of the spatial covariance matrix of the stress glut distribution. This ellipsoid is projected into map-view (left), into the NZ-plane (middle), and into the EZ-plane (right). Bottom row: Instances of the directivity vector representing the instantaneous velocity of the centroid of the source and instances of the Gaussian approximation of the source-time function of the source. Directivity vectors are projected into map-view (left) and the distribution of Z-components of the directivity vectors is plotted as a histogram (middle). Gaussian approximations of the source-time function are plotted relative to the centroid time (right). Gray-scale represents the ensemble of solutions for which, with the exception of the histogram of directivity vector Z-components, darkness represents the density of the plotted solutions. Red represents the mean solution. Blue represents the true solution.

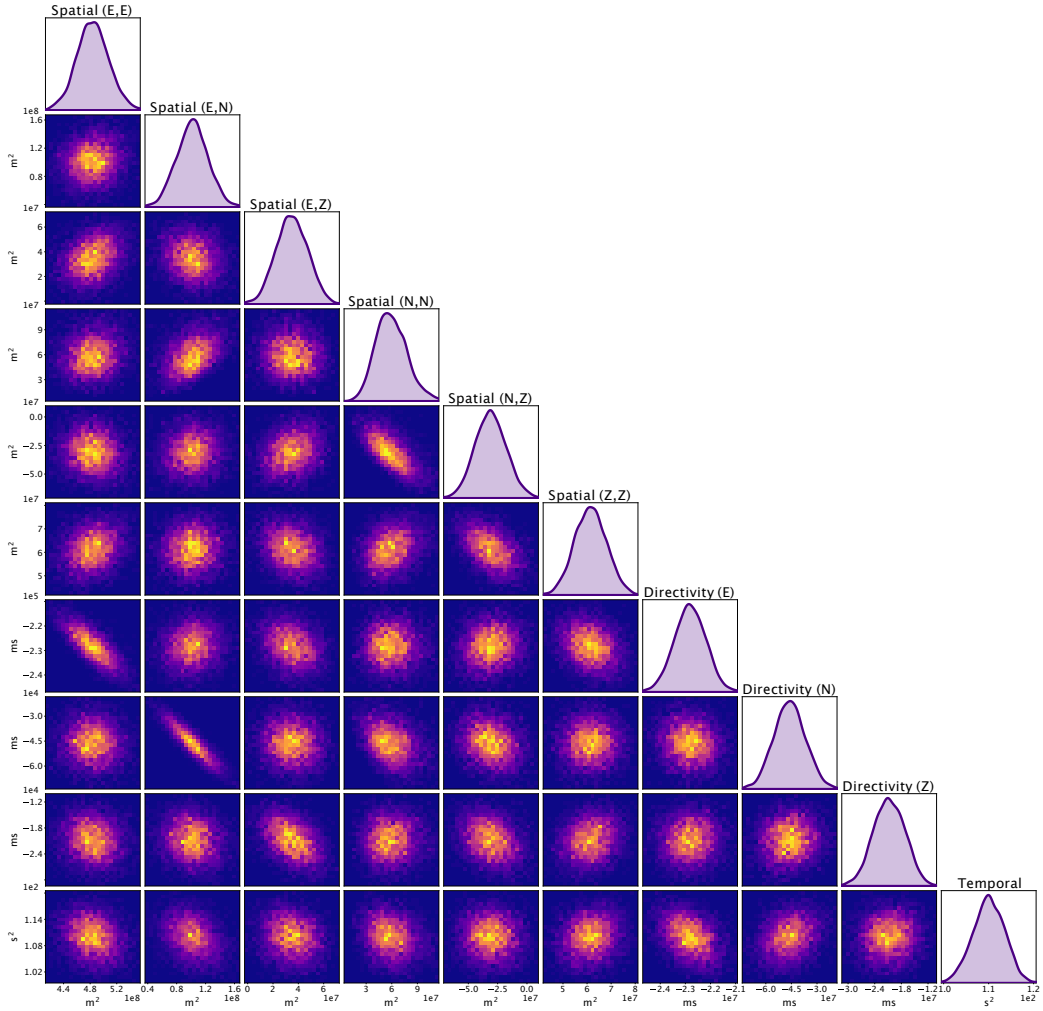

Figure 5. Marginal and joint probability density plots for the 10 independent parameters inverted for in this study. Off-diagonal plots are 2-dimensional histogram plots representing the joint probability distribution for each pair of independent parameters. On-diagonal plots are kernel density estimate plots for the marginal distributions of the adjacent joint probability distributions.

1992) using these chains. The Gelman-Rubin values are far less than 1.1, suggesting that the chains have converged to the target posterior distributions for the second moments. The joint probability distributions for each pair of parameters are shown in Figure 5. The distribution for the hyperparameter σ is shown in Figure S2. As with the synthetic test, these joint distributions show that the inverted parameters are mostly uncorrelated with each other. We can also evaluate the waveform fits for the inversion using real data. These waveform fits are shown in Figure 6. The computed waveforms for the ensemble of solutions inverted for under this framework fit the observed waveforms reasonably well.

Given that some of the features are well resolved, under the assumtion that the stress glut rate is distributed as a 4-dimensional Gaussian function, we can use these ensembles of second moments to constrain features of the fault rupture. In particular, the map-view projection of the volume ellipsoid shown in Figure 7 closely follows the strike of the Oriente Fault, and suggests that 95% of the moment of this event was released in an along-strike length of approximately 90.31 ± 4.59 km. Additionally, the vertical extent of the volume

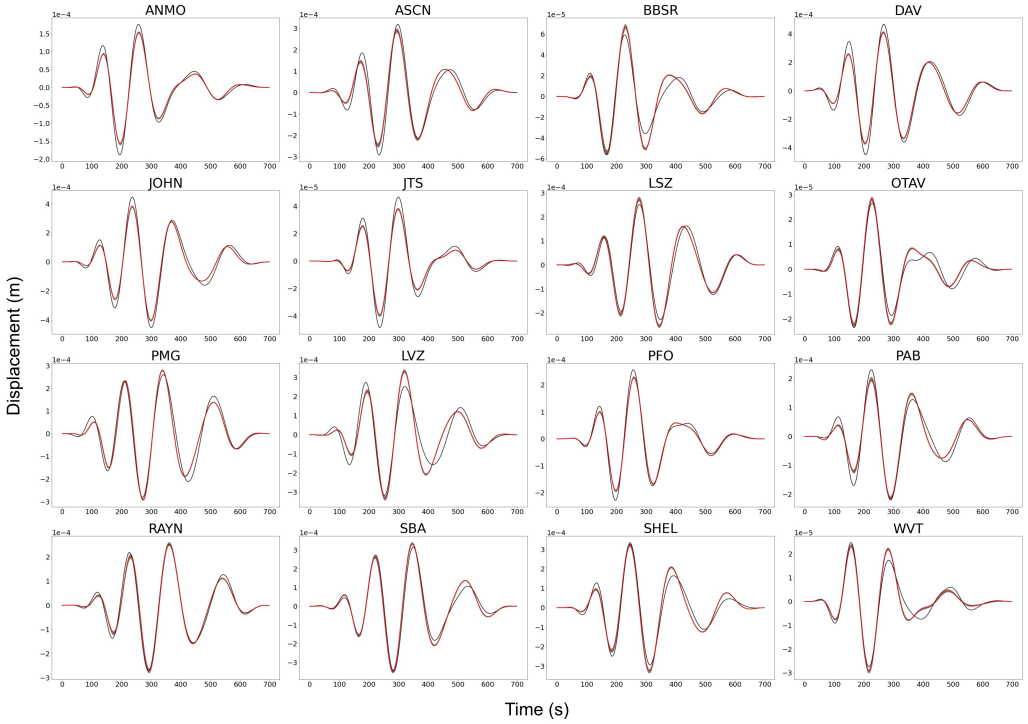

Figure 6. Waveform fits for a subset of the windowed waveforms used in this study. Waveforms are labeled according to the GSN station at which they were recorded. Black waveforms are observations. Gray waveforms are generated using a single solution from the ensemble of solutions from our inversion. Waveforms from each solution in the ensemble are plotted. Red waveforms are generated using the mean solution of the ensemble of solutions from our inversion.

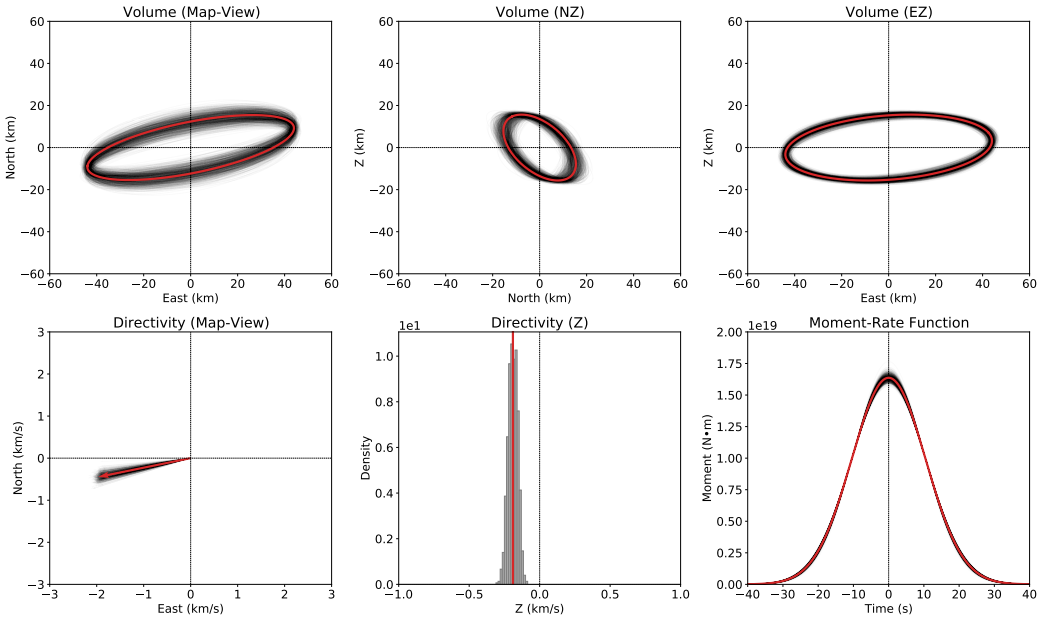

Figure 7. Physically motivated representation of the ensemble of second moment solutions for the 2020 Caribbean event. Top row: Projections of the spatial ellipsoid generated using the eigenvalues and eigenvectors of the spatial covariance matrix of the stress glut distribution. This ellipsoid is projected into map-view (left), into the NZ-plane (middle), and into the EZ-plane (right). Bottom row: Instances of the vector representing the instantaneous velocity of the centroid of the source and instances of the Gaussian approximation of the source-time function of the source. The directivity vectors are projected into map-view (left) and the distribution of Z-components of the directivity vector is plotted as a histogram (middle). Gaussian approximations of the source-time function are plotted relative to the centroid time (right). Gray-scale represents the ensemble of solutions for which, with the exception of the histogram of directivity vector Z-components, darkness represents the density of the plotted solutions. Red represents the mean solution.

ellipsoid suggests that 95% of the moment of this event was released in a depth range of approximately 30.01 ± 3.96 km. The directivity vectors inform both the preferred direction of rupture and the magnitude of the directivity. As illustrated by Figure 7, this event is unilateral to the SW and aligned with the Oriente Fault. Also, there is a smaller Z-directional component in all of the directivity vectors in our ensemble. The magnitude of the directivity measured in this study is approximately 2.128 ± 0.148 km/s to the SW. Finally, under the assumption that the moment of this event was released as a Gaussian distribution in time, the moment-rate functions derived from the temporal second moments from this solution suggest that 95% of the moment for our earthquake was released in a span of 41.92 ± 1.28 seconds.

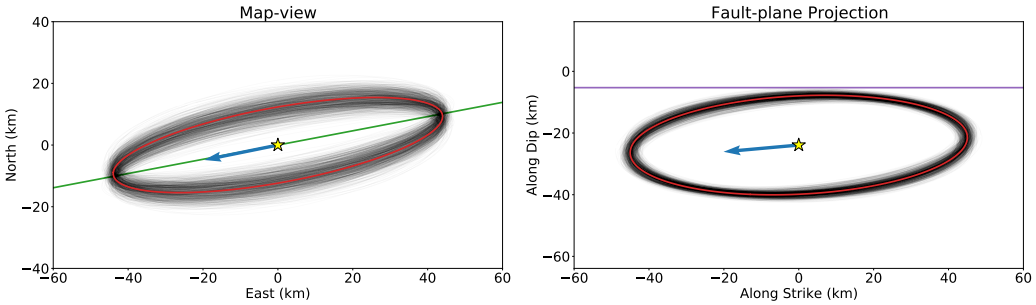

Figure 8. Summary figure of the spatial and directivity features of the 2020 Caribbean Earthquake as derived from the second moment inversion. Left: Map view projection of the second moment ellipsoid and the second moment directivity vector. Gray-scale lines represent the ensemble of solutions and their density. Red line represents the mean solution. Blue vector represents the directivity vector according to the same values shown on the axes but in units of km/s and exaggerated by a factor of 10. Green line represents the true nodal plane from the gCMT solution for the event, which is approximately aligned with the strike of the Oriente Fault. Yellow star represents the centroid position. Right: On-fault projection of the second moment ellipsoid and second moment directivity vector. Line colors match the line colors of the plot to the left. Purple line represents the elevation of the seafloor at the centroid position.

Discussion

In general, the ensemble of solutions for the Caribbean earthquake is well constrained and largely agrees with what is already known about the event. As is shown in Figure 8, the largest principal axis of the ellipsoid representation is well-aligned with the Oriente Fault. Also shown in Figure 8, the directivity vector aligns with the Oriente Fault and suggests a rupture that propagates from the NE to the SW. This unilateral behavior is well-constrained in other estimates of directivity for this source. Additionally, the Gaussian source-time functions for this event suggest that the bulk of the moment release occurs within a span of 40 seconds, and nearly all of the moment release occurs within 80 seconds. This source duration agrees reasonably well with other duration estimates for this source (USGS, 2020; Tadapansawut et al., 2021).

The joint probability distributions shown in Figure 5 suggest that most of the independent parameters of the second moments of the stress glut are uncorrelated. While there are exceptions, this suggests that the lengths of the principal axes of the ellipsoid describing the source volume vary independently. Likewise, changing the magnitude of the directivity along one axis does not necessitate a change of the magnitude of the directivity along another axis. Interestingly, the source duration, determined by the second temporal moment, is uncorrelated with the spatial second moments of the stress glut. This suggests that changing the volume of the source does not imply a change in duration. This non-correlation implies that a change in volume may be correlated with changes in rupture propagation speed and/or directivity. This relationship is partially evidenced by the high correlation between some of the spatial moments with some of the spatiotemporal moments.

The low dimensional second moment estimate of the 2020 Caribbean Earthquake illustrates the unique potential of this methodology for producing probabilistic estimates of finite source properties with few a priori assumptions on the fault geometry and rupture dynamics. The only requirement is a centroid moment tensor solution, which fits nicely into this framework, as the zeroth and first moments represent the scalar moment and centroid position of the earthquake respectively. In fact, the centroid moment tensor solution may be

solved concurrently with the second moment solution, but this introduces nonlinearity and significant additional computational/numerical complexity. The only constraint required in the inversion is that the source be non-negative in extent, which does not exclude any possible source scenarios. However, it is indeed easy to impose additional constraints on the second moments through the use of informed priors on the inversion parameters. Such informed priors should be imposed with the understanding that the second moments describe a covariance matrix of a 4-dimensional Gaussian function. That is, informed priors are not necessarily being placed on the possible source dimensions, but instead are being placed on the possible Gaussian approximations of the source dimensions.

Indeed, the physical representations of these second moment solutions, such as the representation of the Caribbean Earthquake shown in Figure 7, should be interpreted with the understanding that these solutions are probabilistic estimates of Gaussian approximations of the source characteristics. For example, if a spatial extent ellipsoid solution has a vertical extent that exceeds the surface of the Earth, this solution is not necessarily unphysical, but instead may suggest a rupture distribution with a moment release that is biased towards shallower depths. In fact, Gaussian functions only vanish at infinity. The ellipsoid representation extends out to 2σ of the spatial distribution of the stress glut, but the choice of the factor of 2 is to some extent arbitrary. Indeed, for any solution for any earthquake source, there exists an n such that $n\sigma$ exceeds the surface of the Earth with nonzero probability. The spatial and temporal components of the second moment solution should be interpreted from this perspective.

With an understanding of the character of these solutions, we can draw probabilistically motivated conclusions regarding characteristics of the Caribbean Earthquake from these solutions. For example, there are large discrepancies in the along-strike spatial extent of this rupture between fault slip distribution studies. The estimate for the extent of the along-strike rupture most agrees with the USGS finite slip distribution results. That is, we estimate that most of the moment of the earthquake was released within an along-strike distance of approximately 90.31 ± 4.59 km.

One remarkable insight into this earthquake comes from the estimate of the vertical spatial extent of the second moment solution. The solution suggests that the moment release of this earthquake was distributed over a large depth range that spanned approximately 30.01 ± 3.96 km. The GCMT solution for this earthquake places the centroid depth at 23.9 km, which is fairly deep for an oceanic strike-slip earthquake. The large vertical extent estimate suggests that this earthquake ruptured perhaps much deeper than the centroid depth, and thus implies that, as illustrated in Figure 8, the seismogenic zone is thick in this location. This observation may signify that the section of oceanic lithosphere that ruptured is cold (Abercrombie & Ekström, 2001) and may yield insights into the vertical structure and heat flow of ocean-continent transform margins.

Additionally, the directivity metric, the instantaneous velocity of the centroid of the source, is quite large at 2.128 ± 0.148 km/s. The instantaneous velocity of the centroid is identically zero for purely bilateral ruptures and equal to the rupture speed for unilateral ruptures. We can estimate the maximum rupture speed for this event by dividing the square root of the largest eigenvalue of the stress glut spatial covariance with the square root of the stress glut temporal covariance, which yields an average maximum rupture speed of 2.155 km/s. The agreement between the instantaneous velocity of the centroid of this source and the average maximum rupture speed suggests a near purely unilateral rupture for this event.

Conclusions

In this study, we develop a Bayesian framework for computing second moments of the stress glut of earthquakes using teleseismic data. This framework incorporates a positive-definite constraint under Cholesky decomposition and employs Hamiltonian Monte Carlo sampling to efficiently probe the parameter space. This methodology provides robust estimates of uncertainty by sampling the posterior distribution of solutions with dynamic error computation and accounting for the temporal correlation structure in the waveform data. These second moments of the stress glut provide a low-dimensional, physically-motivated representation of source volume, directivity, and duration that requires no *a priori* assumptions and is repeatable and comparable between events. We verify this methodology using a synthetic test and apply this framework to the 2020 M_w7.7 Caribbean earthquake. We show that our solutions for this event provide event parameters that largely agree with the available ground truth. We also show that our solutions can be used to resolve ambiguities between higher-order finite source solutions. Finally, we show that our solution may be used to infer source parameters that have historically been difficult to constrain, such as vertical rupture extent.

Acknowledgments

This work was partially funded by the National Science Foundation's (NSF) Graduate Research Fellowships Program (GRFP) under grant number DGE-1745301. The teleseismic waveforms used in this study are from the Global Seismographic Network (GSN) operated by Scripps Institution of Oceanography (II: IRIS/IDA; https://doi.org/10.7914/SN/II) (Scripps Institution Of Oceanography, 1986) and the Albuquerque Seismological Laboratory (IU: IRIS/USGS; https://doi.org/10.7914/SN/IU) (Albuquerque Seismological Laboratory (ASL)/USGS, 1988). These waveforms and associated metadata used in this study were accessed through the IRIS Data Management Center (DMC). The centroid and moment tensor solution used in this study were obtained from Global Centroid Moment Tensor (gCMT) catalog (Dziewonski et al., 1981; Ekström et al., 2012) at https://www.globalcmt.org/. The synthetic waveforms used in this study were generated using the software Mineos, version 1.0.2 (Masters et al., 2011), available at https://geodynamics.org/cig/software/mineos/ through the Computational Infrastructure for Geodynamics (CIG). Figure 1 was generated using The Generic Mapping Tools (GMT), version 6 (Wessel et al., 2019), available at https://www.generic-mapping-tools.org/.

References

Abercrombie, R. E., & Ekström, G. (2001). Earthquake slip on oceanic transform faults. *Nature*, *410*(6824), 74–77. doi: 10.1038/35065064

Albuquerque Seismological Laboratory (ASL)/USGS. (1988). *Global Seismograph Network (GSN - IRIS/USGS)*. International Federation of Digital Seismograph Networks. Retrieved from `http://www.fdsn.org/doi/10.7914/SN/IU` doi: 10.7914/SN/IU

Ammon, C. J. (2005). Rupture process of the 2004 Sumatra-Andaman Earthquake. *Science*, *308*(5725), 1133–1139. doi: 10.1126/science.1112260

Backus, G., & Mulcahy, M. (1976a). Moment tensors and other phenomenological descriptions of seismic sources–I. Continuous displacements. *Geophysical Journal International*, *46*(2), 341–361. doi: 10.1111/j.1365-246X.1976.tb04162.x

Backus, G., & Mulcahy, M. (1976b). Moment tensors and other phenomenological descriptions of seismic sources–II. Discontinuous displacements. *Geophysical Journal International*, *47*(2), 301–329. doi: 10.1111/j.1365-246X.1976.tb01275.x

Backus, G. E. (1977). Interpreting the seismic glut moments of total degree two or less. *Geophysical Journal International*, *51*(1), 1–25. doi: 10.1111/j.1365-246X.1977.tb04187.x

Bird, P. (2003). An updated digital model of plate boundaries. *Geochemistry, Geophysics, Geosystems*, *4*(3), 297–356. doi: 10.1029/2001GC000252

Bukchin, B. (1995). Determination of stress glut moments of total degree 2 from teleseismic surface wave amplitude spectra. *Tectonophysics*, *248*(3-4), 185–191. doi: 10.1016/0040-1951(94)00271-A

Chen, P. (2005). Finite-moment tensor of the 3 September 2002 Yorba Linda Earthquake. *Bulletin of the Seismological Society of America*, *95*(3), 1170–1180. doi: 10.1785/0120040094

Dahlen, F., & Tromp, J. (1998). *Theoretical global seismology*. Princeton, N.J.: Princeton University Press.

DeMets, C., & Wiggins-Grandison, M. (2007). Deformation of Jamaica and motion of the Gonâve microplate from GPS and seismic data. *Geophysical Journal International*, *168*(1), 362–378. doi: 10.1111/j.1365-246X.2006.03236.x

Du, Y., Aydin, A., & Segall, P. (1992). Comparison of various inversion techniques as applied to the determination of a geophysical deformation model for the 1983 Borah Peak Earthquake. *Bulletin of the Seismological Society of America*, *82*(4), 1840–1866.

Duputel, Z., Agram, P. S., Simons, M., Minson, S. E., & Beck, J. L. (2014). Accounting for prediction uncertainty when inferring subsurface fault slip. *Geophysical Journal International*, *197*(1), 464–482. doi: 10.1093/gji/ggt517

Dziewonski, A. M., & Anderson, D. L. (1981). Preliminary reference earth model. *Geophysical Journal International*, *25*, 297–356.

Dziewonski, A. M., Chou, T. A., & Woodhouse, J. H. (1981). Determination of earthquake source parameters from waveform data for studies of global and regional seismicity. *Journal of Geophysical Research: Solid Earth*, *86*(B4), 2825–2852. doi: 10.1029/JB086iB04p02825

Ekström, G., Nettles, M., & Dziewoński, A. (2012). The global CMT project 2004–2010: Centroid-moment tensors for 13,017 earthquakes. *Physics of the Earth and Planetary Interiors*, *200-201*, 1–9. doi: 10.1016/j.pepi.2012.04.002

GCMT. (2020). *Mw 7.7 cuba region.* Retrieved from `https://www.globalcmt.org/cgi-bin/globalcmt-cgi-bin/CMT5/form?itype=ymd&yr=2020&mo=1&day=1&otype=ymd&oyr=2020&omo=2&oday=1&jyr=1976&jday=1&ojyr=1976&ojday=1&nday=1&lmw=7.5&umw=10&lms=0&ums=10&lmb=0&umb=10&llat=-90&ulat=90&llon=-180&ulon=180&lhd=0&uhd=1000&lts=-9999&uts=9999&lpe1=0&upe1=90&lpe2=0&upe2=90&list=0`

Gelman, A., Carlin, J., Stern, H., Dunson, D., Vehtari, A., & Rubin, D. (2010). *Bayesian data analysis.* Boca Raton, F.L.: Chapman and Hall-CRC Press.

Gelman, A., & Rubin, D. (1992). Inference from iterative simulation using multiple sequences. *Statistical Science*, *7*(4), 457–511.

Hartzell, S. H., & Heaton, T. H. (1983). Inversion of strong ground motion and teleseismic waveform data for the fault rupture history of the 1979 Imperial Valley, California Earthquake. *Bulletin of the Seismological Society of America*, *73*(6), 1553–1583.

Ide, S., Baltay, A., & Beroza, G. C. (2011). Shallow Dynamic Overshoot and Energetic Deep Rupture in the 2011 Mw 9.0 Tohoku-Oki Earthquake. *Science*, *332*(6036), 1426–1429. doi: 10.1126/science.1207020

Innes, M. (2019). Don't Unroll Adjoint: Differentiating SSA-Form Programs. *arXiv:1810.07951 [cs]*.

Lay, T. (2018). A review of the rupture characteristics of the 2011 Tohoku-oki Mw 9.1 earthquake. *Tectonophysics*, *733*, 4–36. doi: 10.1016/j.tecto.2017.09.022

Lee, E., Chen, P., Jordan, T. H., & Wang, L. (2011). Rapid full-wave centroid moment tensor (CMT) inversion in a three-dimensional earth structure model for earthquakes in Southern California: Rapid full-wave CMT inversion. *Geophysical Journal International*, *186*(1), 311–330. doi: 10.1111/j.1365-246X.2011.05031.x

Mann, P., Taylor, F., Edwards, R., & Ku, T.-L. (1995). Actively evolving microplate formation by oblique collision and sideways motion along strike-slip faults: An example from the northeastern Caribbean plate margin. *Tectonophysics*, *246*(1-3), 1–69. doi: 10.1016/0040-1951(94)00268-E

Masters, G., Woodhouse, J., & Freeman, G. (2011). *Mineos.* Retrieved from `https://geodynamics.org/cig/software/mineos/`

McGuire, J. J. (2004). Estimating Finite Source Properties of Small Earthquake Ruptures. *Bulletin of the Seismological Society of America*, *94*(2), 377–393. doi: 10.1785/0120030091

McGuire, J. J., Zhao, L., & Jordan, T. H. (2000). Rupture dimensions of the 1998 Antarctic Earthquake from low-frequency waves. *Geophysical Research Letters*, *27*(15), 2305–2308. doi: 10.1029/1999GL011186

McGuire, J. J., Zhao, L., & Jordan, T. H. (2001). Teleseismic inversion for the second-degree moments of earthquake space-time distributions. *Geophysical Journal International*, *145*(3), 661–678. doi: 10.1046/j.1365-246x.2001.01414.x

McGuire, J. J., Zhao, L., & Jordan, T. H. (2002). Predominance of Unilateral Rupture for a Global Catalog of Large Earthquakes. *Bulletin of the Seismological Society of America*, *92*(8), 3309–3317. doi: 10.1785/0120010293

Meng, H., McGuire, J. J., & Ben-Zion, Y. (2020). Semiautomated estimates of directivity and related source properties of small to moderate Southern California earthquakes using second seismic moments. *Journal of Geophysical Research: Solid Earth*, *125*(4), e2019JB018566. doi: 10.1029/2019JB018566

Minson, S. E., Simons, M., & Beck, J. L. (2013). Bayesian inversion for finite fault earthquake source models I—theory and algorithm. *Geophysical Journal International*, *194*(3), 1701–1726. doi: 10.1093/gji/ggt180

Monelli, D., Mai, P. M., Jónsson, S., & Giardini, D. (2009). Bayesian imaging of the 2000 Western Tottori (Japan) earthquake through fitting of strong motion and GPS data. *Geophysical Journal International*, *176*(1), 135–150. doi: 10.1111/j.1365-246X.2008.03943.x

Moreno, B., Grandison, M., & Atakan, K. (2002). Crustal velocity model along the southern Cuban margin: implications for the tectonic regime at an active plate boundary. *Geophysical Journal International*, *151*(2), 632–645. doi: 10.1046/j.1365-246X.2002.01810.x

Moreno, M., Rosenau, M., & Oncken, O. (2010). 2010 Maule earthquake slip correlates with pre-seismic locking of Andean subduction zone. *Nature*, *467*(7312), 198–202. doi: 10.1038/nature09349

Neal, R. (2010). *MCMC using Hamiltonian dynamics*. Boca Raton, F.L.: Chapman and Hall-CRC Press.

Ross, Z. E., Idini, B., Jia, Z., Stephenson, O. L., Zhong, M., Wang, X., ... Jung, J. (2019). Hierarchical interlocked orthogonal faulting in the 2019 Ridgecrest earthquake sequence. *Science*, *366*(6463), 346–351. doi: 10.1126/science.aaz0109

Saito, T., Ito, Y., Inazu, D., & Hino, R. (2011). Tsunami source of the 2011 Tohoku-Oki earthquake, Japan: Inversion analysis based on dispersive tsunami simulations. *Geophysical Research Letters*, *38*(7), L00G19. doi: 10.1029/2011GL049089

Scripps Institution Of Oceanography. (1986). *IRIS/IDA Seismic Network*. International Federation of Digital Seismograph Networks. Retrieved from `http://www.fdsn.org/doi/10.7914/SN/II` doi: 10.7914/SN/II

Tadapansawut, T., Okuwaki, R., Yagi, Y., & Yamashita, S. (2021). Rupture Process of the 2020 Caribbean Earthquake Along the Oriente Transform Fault, Involving Supershear Rupture and Geometric Complexity of Fault. *Geophysical Research Letters*, *48*(1), e2020GL090899. doi: 10.1029/2020GL090899

Tarantola, A. (2005). *Inverse Problem Theory and Methods for Model Parameter Estimation*. Philidelphia, P.A.: Society for Industrial and Applied Mathematics.

USGS. (2020). *M 7.7-123km nnw of lucea, jamaica.* Retrieved from `https://earthquake.usgs.gov/earthquakes/eventpage/us60007idc/executive`

Van Dusen, S. R., & Doser, D. I. (2000). Faulting processes of historic (1917–1962) M 6.0 earthquakes along the North-central Caribbean margin. *Pure and Applied Geophysics*, *157*(5), 719–736. doi: 10.1007/PL00001115

Wald, D. J., & Heaton, T. H. (1992). Spatial and temporal distribution of slip for the 1992 Landers, California, Earthquake. *Bulletin of the Seismological Society of America*, *84*(3), 668–691.

Walsh, D., Arnold, R., & Townend, J. (2009). A Bayesian approach to determining and parametrizing earthquake focal mechanisms. *Geophysical Journal International*, *176*(1), 235–255. doi: 10.1111/j.1365-246X.2008.03979.x

Wessel, P., Luis, J. F., Uieda, L., Scharroo, R., Wobbe, F., Smith, W. H. F., & Tian, D. (2019). *The generic mapping tools.* Retrieved from `https://www.generic-mapping-tools.org/`

Wéber, Z. (2006). Probabilistic local waveform inversion for moment tensor and hypocentral location. *Geophysical Journal International*, *165*(2), 607–621. doi: 10.1111/j.1365-246X.2006.02934.x